Brazilian Journal
of Chemical
Engineering

ISSN 0104-6632
Printed in Brazil
www.abeq.org.br/bjche

Vol. 36, No. 03, pp. 1119 - 1129, July - September, 2019
dx.doi.org/10.1590/0104-6632.20190363s20180531

MODELING AND SIMULATION OF A VACUUM MEMBRANE DISTILLATION PLANT COUPLED WITH SOLAR ENERGY AND USING HELICAL HOLLOW FIBERS

Adel Zrelli[1,2*] and Béchir Chaouachi[2]

[1] University of Gabes, High Institute of Applied Sciences and Technology of Gabes, Gabes, Tunisia.
E-mail: adel.zrelli@yahoo.fr - ORCID: 0000-0003-3471-002X
2 University of Gabes, National Engineering School of Gabes, Environmental, Catalysis and Process Analysis Research Unity, Gabes, Tunisia.

(Submitted: November 6, 2018 ; Revised: March 10, 2019 ; Accepted: March 28, 2019)

Abstract - This paper investigates the effect of operating conditions such as coil pitch, fiber diameter, distance between fiber and absorber internal wall and absorber diameter for a vacuum membrane installation coupled with solar energy and using helically coiled fiber to maximize the permeate flow rate. The model is based on a system of equations composed of two-dimensional Navier-Stokes equations. Matlab and FemLab were used to solve this system of equations. The results showed that the best values of fiber geometric configuration are 3.22 cm for the coil pitch, 6 mm for the fiber diameter, 4.3 mm for the distance between the fiber and the absorber internal wall and 14 cm for the absorber diameter. For this configuration, the permeate flow rate is 18.6 10^{-5} kg/s. In conclusion, these results are important in the membrane module design for practical membrane distillation applications.
Keywords: Vacuum membrane distillation; Helical fiber; Solar energy; Heat and mass transfer; Simulation.

INTRODUCTION

Membrane distillation (MD) is a thermally driven separation process. In this process, only vapor molecules pass through a porous and hydrophobic membrane. Qtaishat and Banat (2013) classified MD into four configurations. The first configuration is the direct contact membrane distillation (DCMD). For the DCMD, the cooling solution is in direct contact with the permeate side of the membrane (Andrjesdóttir et al., 2013; Nakoa et al., 2016; Nariyoshi et al., 2016). The air gap membrane distillation (AGMD) is the second configuration. For this configuration, the vapor phase crosses a stagnant air gap and condenses on a surface inside the module (Khayet, 2011; Singh and Sirkar, 2012). *The* third configuration is the sweeping gas membrane distillation (SGMD). A sweeping gas is driving the produced vapor outside the membrane module to condensate this vapor (Shirazi et al., 2015). Wang et al. (2015) and Joo et al. (2016) present the configuration of the vacuum membrane distillation (VMD). In this configuration, a vacuum carries the vapor phase through the membrane and its condensation will be outside of the membrane. When comparing VMD to the conventional distillation processes, many advantages are noted for VMD such as low operating temperature (Frikha et al., 2017). In addition, the VMD configuration present two principal advantages when compared to the other MD configurations. These advantages are low mass transfer resistance and reduced conductive heat loss (Safavi and Mohammadi, 2009). These advantages imply an improvement in heat and mass transfer.

Due to these advantages, we note an increase in using VMD in various applications. Moreover, the efficiency of this configuration can be enhanced by

* Corresponding author: Adel Zrelli - E-mail: adel.zrelli@yahoo.fr

the use of an energy recovery system. This increase in efficiency is due to the decrease in the energy consumption for this configuration. According to Cabassud and Wirth (2003), this energy consumption decreases from 100 to 1.3 kWh/m^3 with the use of a free heating source like solar energy.

To couple VMD with solar energy, the membrane can be placed inside or outside the absorber of the solar collector. In the first case, we need a single loop in which the feed solution is directly heated in the absorber of the solar collector. For the second case, there are two loops, which are the collector loop and the desalination loop. In the collector loop, the solar collector heats a fluid and the latter heats the feed solution, for the desalination loop, with a heat exchanger.

Furthermore, membranes used for VMD have two main types of configurations, which are flat membrane and hollow fiber membrane. For the hollow fiber membrane, we find the linear hollow fiber and the helical hollow fiber.

Few studies are interested in the simulation and experimentation of helical fibers. Yücel and Çulfaz-Emecen (2018) have compared, for the filtration of yeast, the performance of the helical hollow fiber to that of the linear hollow fiber. After experimentation, they noted an improvement of the antifouling behavior for the helical hollow fiber. This implies a decrease of fouling resistance and so an increase of flux for the helical hollow fiber. Regarding DCMD, the work of Ali et al. (2015) is of great interest. They used three hollow fiber configurations, which are linear, wavy and helical. The experiments were performed with whey as feed solution. This solution flows inside the hollow fiber and has Re about 160 and inlet temperature of 54°C. Under these conditions, a flux enhancement of 47% can be observed for the helical hollow fiber when compared to the linear hollow fiber flux. This enhancement is due to the increase of the temperature polarization coefficient for the case of the helical hollow fiber.

Mendez et al. (2019) carried out a study in which they investigated the effect of membrane material and passive techniques by modifying the geometry of the fiber to enhance water flux. For the case of the feed flow in the lumen side of the hollow fiber, an increase of about 20% in water flux was remarked for the helical hollow fiber when compared to the linear hollow fiber. This increment is explained by the provoked turbulence on the membrane surface. Thus, this induces an increase of the temperature polarization coefficient, which implies an enhancement of thermal efficiency. In the same case, Zrelli et al. (2014) confirmed the use of helical coiled fiber for the VMD. This confirmation was shown following the comparison of the performance of helical coiled fiber to linear. The results showed an improvement of the permeate flow rate, for the case of the helical coiled fiber, about 28%.

In this work, an investigation of effects of operating parameters such us coil pitch, distance between fiber and absorber internal wall, fiber diameter and absorber diameter on the permeate flow rate for a solar vacuum membrane distillation installation equipped with helical coiled fiber is presented. In addition, the determination of the value of each parameter allowing the maximum permeate flow rate has been done. To achieve this aim, a mathematical model was developed that combined non-linear mass and heat transfer equations. These equations have been solved using Matlab and Femlab software.

MATERIAL AND METHODS

Installation plan

In this work, we introduced two helical coiled fibers in the solar concentrator absorber. After that, this absorber was mounted on the focal axis of a parabolic trough concentrator (Figure1). Due to this design, the membrane and the absorber have the same configuration as that of the helical heat exchanger

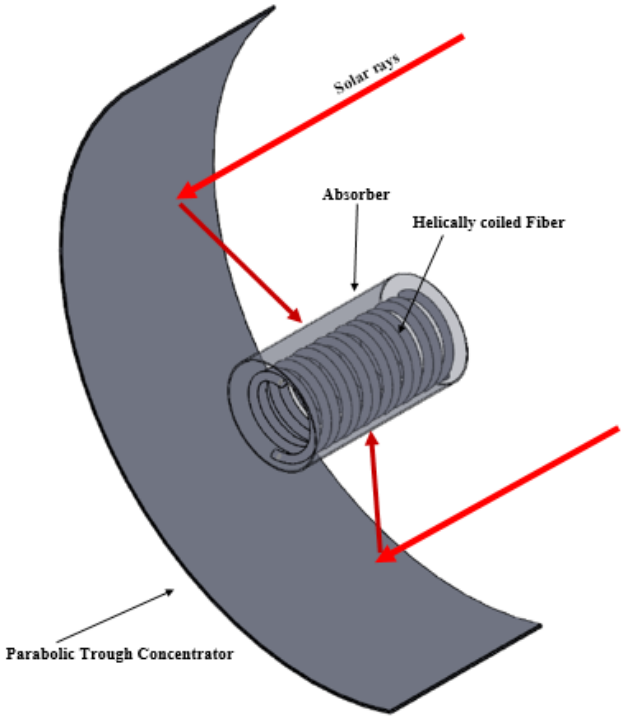

Figure 1. Schematic layout of the thermal solar membrane distillation (TSMD).

Mathematical model.

Owing to the configuration of the thermal solar membrane distillation installation (TSMD), we have a symmetric flow about a vertical plane passing through the axis of the absorber, which leads to study only the half-plane (Figure 2). To define and simplify the model, the following assumptions were assumed:

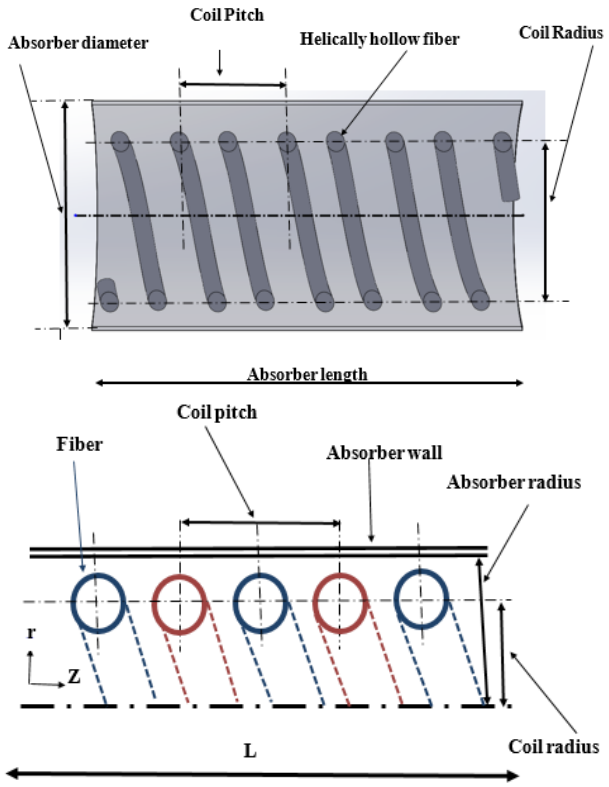

Figure 2. 3-D and 2-D Longitudinal section of the absorber with helical coiled fibers.

1. The motion is considered as axisymmetric, hence, the model only need to consider the half of the absorber
2. The flow is fully developed before entering the absorber.
3. Steady state is assumed for all simulations
4. No slip condition is valid on the surface of the fiber.
5. The fluid is Newtonian and incompressible.
6. All angular gradient parameters are negligible; the model is described in the coordinates r and z.
7. The gravity force was neglected.

Governing equations

By considering these assumptions, the appropriate governing equations were expressed as follows (Bird et al., 2002).

The continuity equation was expressed as:

$$\frac{\partial u_r}{\partial r}+\frac{u_r}{r}+\frac{\partial u_z}{\partial z}=0 \tag{1}$$

The parameters u_r and u_z were the radial and axial feed velocity, m/s.

Momentum equations:

$$u_r\frac{\partial u_r}{\partial r}+u_z\frac{\partial u_r}{\partial z}=\nu\left[\frac{\partial}{\partial r}\left(\frac{1}{r}\frac{\partial r u_r}{\partial r}\right)+\frac{\partial^2 u_r}{\partial z^2}\right] \tag{2}$$

$$u_r\frac{\partial u_z}{\partial r}+u_z\frac{\partial u_z}{\partial z}=-\frac{1}{\rho}\frac{\partial P}{\partial z}+\nu\left[\frac{1}{r}\frac{\partial}{\partial r}\left(r\frac{\partial u_z}{\partial r}\right)+\frac{\partial^2 u_z}{\partial z^2}\right] \tag{3}$$

where P, ρ and ν were the feed pressure (Pa), the feed kinematic viscosity (m^2/s), and the feed density, kg/m^3.

Energy equation:

$$u_r\frac{\partial T}{\partial r}+u_z\frac{\partial T}{\partial z}=\alpha\left[\frac{1}{r}\frac{\partial}{\partial r}\left(r\frac{\partial T}{\partial r}\right)+\frac{\partial^2 T}{\partial z^2}\right] \tag{4}$$

The parameters T and α were the temperature (K), and the thermal diffusivity (m^2/s) of the feed, respectively.

The boundary conditions for the velocity and the temperature are:

At the inlet of the absorber, Z=0:

$$u_z=2u_0\left(1-\left(\frac{r}{R}\right)^2\right)$$
$$u_r=0 \tag{5}$$
$$T=T_{in}$$

The parameters T_n, R and u_0 were the feed temperature at the inlet of the absorber (K), the absorber radius (m), the average feed velocity at the inlet of the absorber, m/s.

At the exit, Z=L:

$$u_r=\frac{\partial u_z}{\partial z}=\frac{\partial T}{\partial z}=0 \tag{6}$$

At the hollow fiber membrane surface:

$$u_z=0$$
$$u_r=0 \tag{7}$$
$$T=T_{inter}$$

At the absorber interior wall, r=R:

$$u_z=0$$
$$u_r=0 \tag{8}$$
$$T=T_w$$

The temperature at the absorber interior wall was T_w, (K).

Heat transfer model

The bulk temperature (T_{bulk}, (K)) is related to the feed/membrane interface (T_{inter}, (K)) by the following heat balance equation (Mericq et al., 2010; Qtaishat and Banat, 2013):

$$J_v L_v = h_f \left(T_{bulk} - T_{inter}\right) \quad (9)$$

where J_v was the permeate flux, kg/(m²s).

Based on the equation below (Salimpour, 2009, 2008), the heat transfer coefficient at the outside of the hollow fiber (h_f, (W/(m²K)) was calculated:

$$Nu = 19.64\,Re^{0.513}\,Pr^{0.129}\,\gamma^{0.938} \quad (10)$$

which is valid for helical configuration, 60<Re<550, 0.058<γ<0.095, 5<Pr<7, where $\gamma = P/2\pi R_c$.

Chaouchi et al. (2007) expressed the water latent heat of vaporization (L_v, (kJ/kg)) by:

$$Lv = 2538.2 - 2.91 T_{inter} \quad (11)$$

The equation below gives the interior wall temperature of the absorber (T_w):

$$T_w = T_e - \frac{q_u e}{\lambda_m} \quad (12)$$

where T_e, q_u, e and λ_m were the absorber exterior wall temperature (K), useful heat flow (W/m²), thickness of the wall absorber (m) and thermal conductivity of the absorber enlightened face (W/(m K)), respectively, and q_u is given by:

$$q_u = q_a - q_e \quad (13)$$

where q_a is the incident power of the absorber radiance (W/m²) expressed by:

$$q_a = I C_g \rho\gamma\alpha\tau \quad (14)$$

The parameters I, C_g, ρ, γ, α, and τ were the incident radiation on the level of the concentrator (W/m²), geometric concentration (-), reflectivity coefficient of the concentrator (-), interception coefficient of absorber (-), absorption coefficient of absorber (-), and transmission coefficient of the glass cover of absorber (-).

The sum of the heat losses by radiation and convection between the surroundings and the absorber, q_e (W/m²), is given by (Chaouchi et al., 2007):

$$q_e = \varepsilon_a \sigma (T_e^4 - (T_a - 11)^4) + (5.7 + 3.8 w_s)(T_e - T_a) \quad (15)$$

The parameters ε_a, σ, w_s, T_e and T_a were the emissivity of the absorber (-), Stefan-Boltzmann constant (W/m²K⁴), wind velocity (m/s), absorber external wall temperature (K), and ambient temperature (K) respectively.

The heat balance equation of the absorber "*j*" element (Figure 3) is:

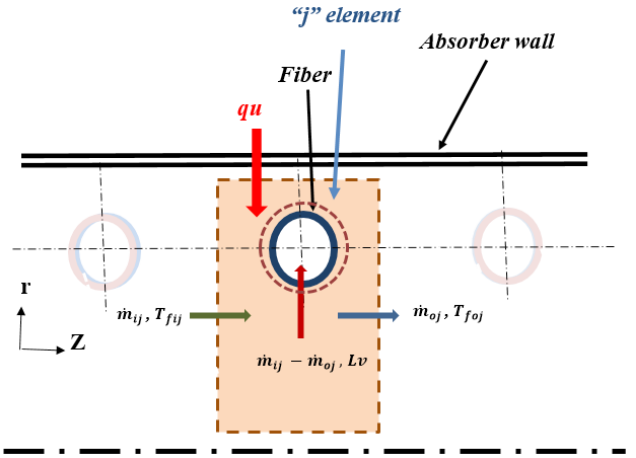

Figure 3. Thermal balance on the "*j*" element of the absorber.

$$q_u s_j + \dot{m}_{ij} Cp T_{fij} - \dot{m}_{oj} Cp T_{foj} - (\dot{m}_{ij} - \dot{m}_{oj}) Lv = 0 \quad (16)$$

where S_j, m_{oj}, C_p, T_{foj}, m_{ij}, and T_{fij} were the outer side surface of the element "*j*" of the absorber (m²), feed flow rate in the outlet of element "*j*" (kg/s), specific heat of the feed (kJ/(kg K)), temperature of fluid at the exit of the element "*j*" of the absorber (K), feed flow rate in the inlet of element "*j*" (kg/s), and temperature of fluid, at the entrance of the element "*j*" of the absorber (K).

Mass transfer model

For vacuum membrane distillation, the prevailing mechanism of mass transfer is the Knudsen mechanism. In this case, there is a linear relationship between the permeate flux (J_v) and the water vapor pressure difference through the membrane (ΔP (Pa)) (Izquierdo-Gil and Jonsson, 2003):

$$J_V = \frac{k_m}{\sqrt{M_w}} \Delta P = \frac{k_m}{\sqrt{M_w}} \left(P_{inter} - P_v\right) \quad (17)$$

The parameters k_m, M_w, P_{inter}, and P_v were the membrane permeability coefficient (s mole$^{1/2}$ m^{-1} kg$^{-1/2}$), water molar mass (kg/mol), water vapor pressure at the liquid/vapor interface (Pa), and vacuum pressure (Pa), respectively.

Cabassud and Wirth (2003) expressed, in the Knudsen type of flow, the membrane permeability coefficient (k_m) by:

$$k_m = 1.064 \frac{r\varepsilon}{\delta\tau} \sqrt{\frac{1}{RT}} \quad (18)$$

where δ, τ, ε and r were, respectively, the membrane thickness (m), pore tortuosity (-), membrane porosity (-) and pore radius (m).

The water vapor pressure (P_{inter}) at the liquid/vapor interface can be evaluated using Antoine's equation (Mengual et al., 2004):

$$P_{inter}(T) = \exp\left(23.1964 - \frac{3816.44}{T - 46.13}\right) \quad (19)$$

where $P_{inter}(T)$ is in Pa and T is in K.

The permeate flow rate, m_{pj} (kg/s), for each "j" element of the absorber is calculated as:

$$\dot{m}_{pj} = J_{vj}\pi L d_o \quad (20)$$

where L is the module length (m), and d_o is the outer diameter of the fiber (m).

Solution procedure

The continuity, momentum and, energy equations Eqs. (1)-(4) were discretized by a finite element method. According to the algorithm supplied in Fig. A1 given in the Appendix, the iteration procedure employed to solve the coupled equations of hydrodynamics and heat transfer was the following:

- ✓ the velocity profile and the temperature in the absorber's inlet is specified.
- ✓ to determine the temperature distribution, all the membrane interfaces temperatures and the elementary external wall absorber temperatures are guessed.
- ✓ the absorber interior wall temperature (T_w) was determined by resolving the system of equations (12)-(15).
- ✓ the energy equation, Eq.(4), at the boundary conditions, Eqs.(5)-(8), was solved to get the bulk temperature for the first element of the fiber.
- ✓ the membrane interface temperature for the first element of the fiber was calculated by resolving the nonlinear system of equations (9)-(11), (17)-(19).
- ✓ the resulting temperature was compared to the guessed value. If the difference was greater than the tolerance limit (3×10^{-3} %), the procedure was reiterated with a new guess for the membrane interface temperature, being the calculated value. When the difference between the two temperature values was within the prescribed limit, the corresponding temperature was taken as a boundary condition. Then the permeate flux of the fiber element number "1" (J_{v1}) and the permeate flow rate "m_{p1}" can be determined. If the difference between "m_{p1}" and the value of "m_{i1} - m_{o1}", given by Eq. (16), was greater than the tolerance limit (2%), a new guess for the elementary external wall temperature is applied. When the difference between the two values of the flow rates was within the prescribed limit, the permeate flow rate was determined. This procedure is then repeated for all elements of the absorber.

All these steps were carried out on a PC with a CPU 5500U 2.4 GHz processor running under Windows 10. The computed results were done using MATLAB and FemLab.

RESULTS AND DISCUSSION

In Table 1, the values of the operating characteristics and design specifications of the membrane module are presented. In addition, Table 2 presents the absorber optical and geometrical parameters values. Based on these values, we present the results of our study in order to enhance the heat and mass transfer performance and to maximize the permeate flow rate. These results concern the best values of the geometrical characteristics of the TSMD.

Table 1. Operating characteristics and design specifications of the membrane module.

Property	Value
Number of fibers	2
Length of the module (mm)	233
Vacuum pressure (Pa)	1000
Inlet feed velocity (m/s)	$3.4\ 10^{-4}$ (Re=68)
Inlet feed temperature (°C)	20

Table 2. Optical and geometrical parameters of the absorber and concentrator (Gallet et al., 1980 ; Sacadura, 1980 ; Gong et al, 2017).

Parameter	Value
Absorptivity of the absorber	0.9
Reflectivity of the concentrator	0.9
Transmissivity of the absorber glass cover	1
Intercept factor	0.9
Emissivity of absorber	0.9
Length of the absorber (m)	0.233

Effect of the coil pitch of the helically coiled fiber

Figure 4 (a) shows the permeate flow rate evolution with the coil pitch. This evolution seems to be parabolic with a maximum towards the value of 32.2 mm for the pitch. When the pitch decreases, the size of the wake decreases too. This induces a decrease in the space between the fibers available for bulk flow and a drop in the feed velocity and the Reynolds number. In this case, the boundary layer heat transfer coefficient and the permeate flux decreased. In addition, a drop of the pitch implies an increase of the exchange surface of the fiber (Figure 4 (b)). These two variations, of permeate flux and fiber exchange surface, lead to getting the best pitch which is 32.2 mm that maximizes the permeate flow rate.

Effect of the distance between internal wall of the absorber and fiber

Figure 5 presents the effect of the distance between the internal wall of the absorber and fiber (or the coil radius) on the permeate flow rate. According to this

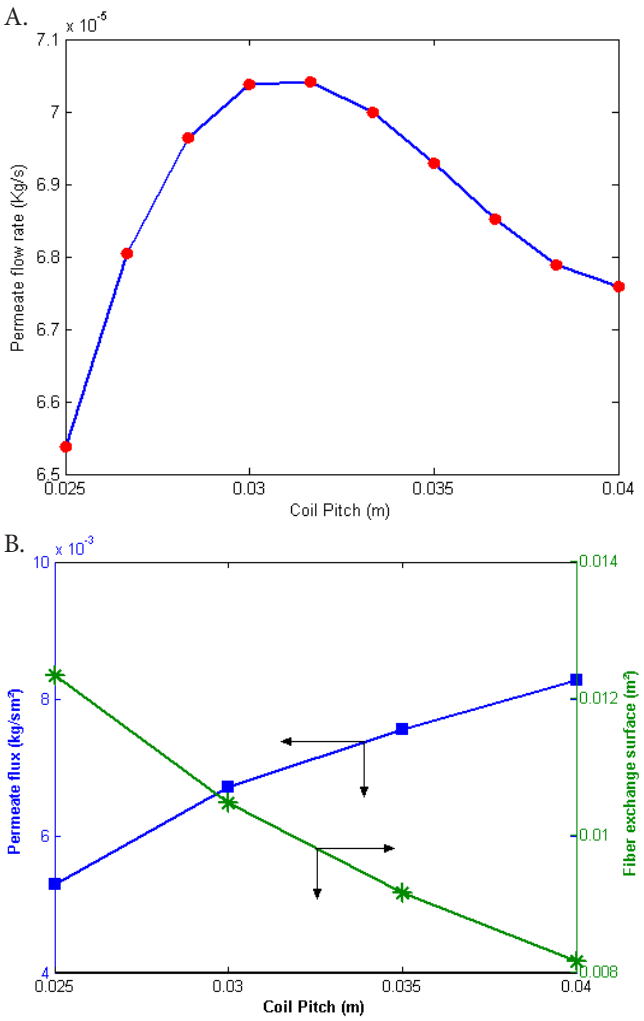

Figure 4. Effect of coil pitch on (a) Permeate flow rate, (b) Permeate flux and fiber exchange surface.

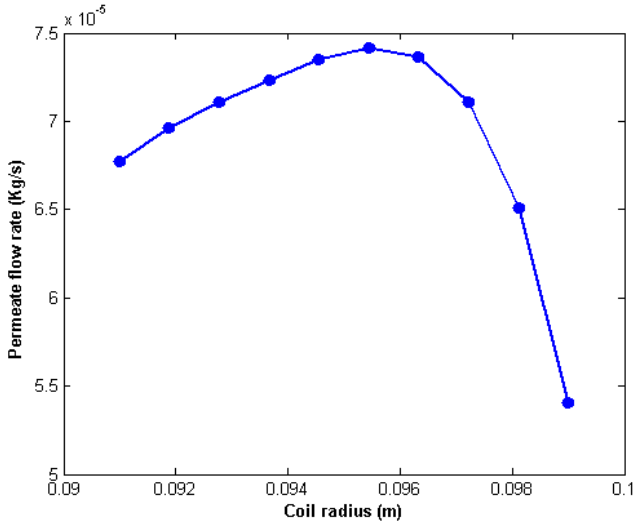

Figure 5. Evolution of permeate flow rate with coil radius.

figure, the effect of the coil radius on the permeate flux is clear. By increasing the coil radius, the permeate flux increases to reach the greatest value toward 95.7 mm. This value of coil radius corresponds to the value of 4.3 mm for distance between the internal wall of the absorber and fiber. This shows that the feed velocity controls the permeate flux. This velocity decreases with the decrease of the channel width between the interior wall of the absorber and the outside face of the fiber. When the value of this width decreases, we noted the effect of channel blockage. In addition, the parabolic profile of the feed velocity led to obtaining decreased values of velocity nears the absorber interior wall.

Effect of the fiber diameter of the helically coiled fiber

In this case, the diameter value of the helically coiled fiber was varied between 0.5 and 8.5 mm, lefting unchanged the other characteristics. Figure 6 shows the obtained permeate flow rate and permeate flux for these different diameters. According to this figure, the permeate flow rate increases as the diameter increases from 0.5 to 6 mm and decreases after that.

The membrane exchange surface also increases with the increase of the fiber diameter. This allowed us to have a high flux of the fibers with smaller diameters. This flow tends to decrease with increasing diameter fiber. To explain the evolution of the permeate flow rate with the fiber diameter, the variations of the difference between the temperatures of bulk and interface (Figure 7 (a)), the exchange surface of the membrane (Figure 7 (b)) and the membrane outside heat transfer coefficient (Figure 7 (c)) are plotted. Based on these figures, when the fiber diameter increases, the heat transfer coefficient on the outside of the membrane and the difference (T_{bulk}-T_{inter}) decrease. In contrast, the exchange surface of the membrane increases. These changes can be explained by the fact that, if we keep the same characteristics of the fiber and only we change the fiber diameter, the space between two contiguous coils

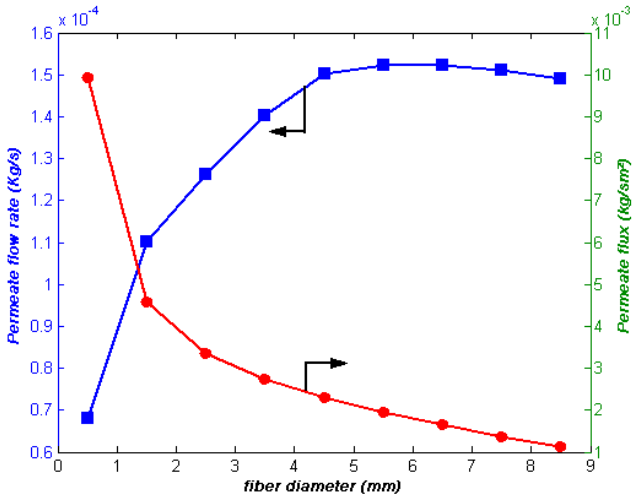

Figure 6. Variations of permeate flow rate and permeate flux as a function of coil radius.

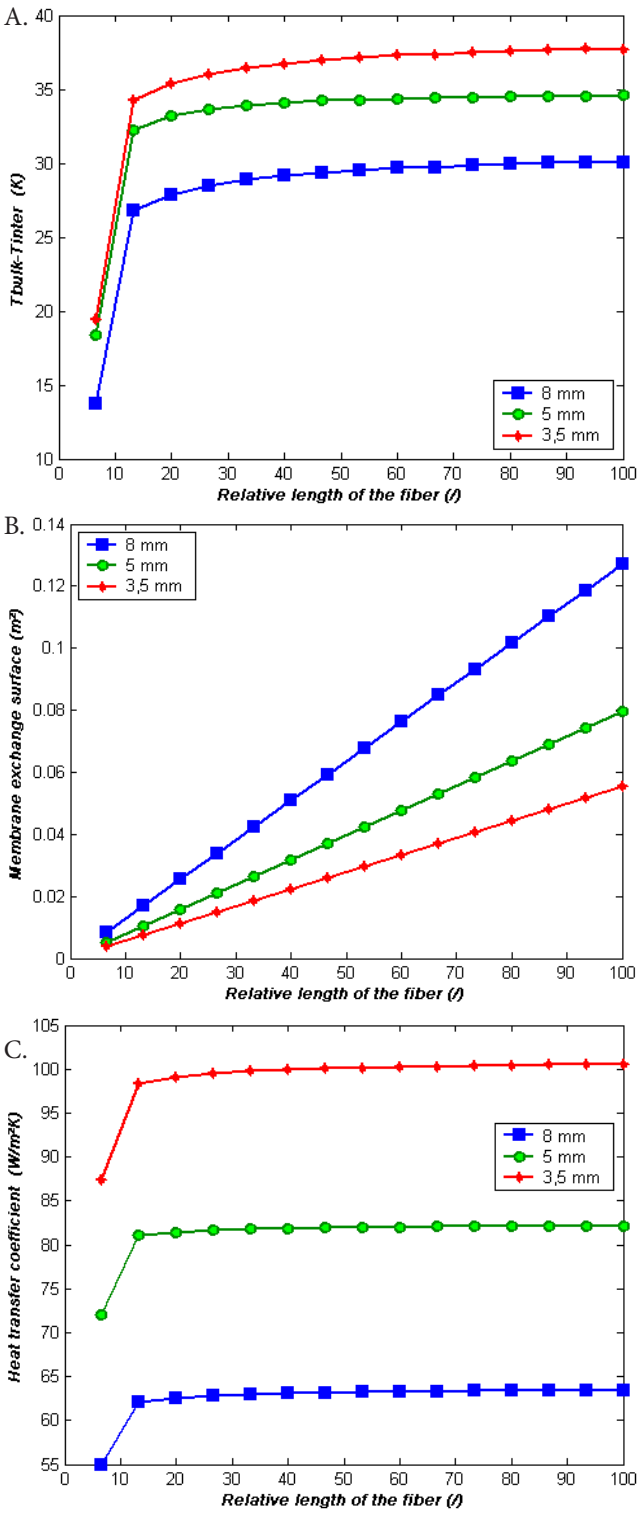

Figure 7. Effect of relative length of the fiber on (a) T_{bulk}-T_{inter}, (b) Membrane exchange surface, (c) Heat transfer coefficient.

decreases. Also, the space between the interior wall of the absorber and the outside face of the fiber decreases too. Thus, the turbulence of the feed decreases, which leads to a fall in the coefficient of heat transfer from the wall to the feed. So, the bulk temperature recorded a significant drop. A similar trend was found for the heat transfer coefficient between the bulk and the membrane interface decreases. So T_{inter} will reach a lower value and the difference between T_{bulk} and T_{inter} will reduce. This proves the decrease of the permeate flux. As noted, the membrane exchange surface increases with increasing fiber diameter. Also, the permeate flow rate is only the product of the membrane surface with the permeate flux. When the fiber diameter increases the membrane exchange surface increases, and the permeate flux decreases. These two variations allow the permeate flow rate to go through a maximum point. This point corresponds to the best fiber diameter for which the permeate flow is maximized. In our case, this best value of fiber diameter is 6 mm

Effect of the absorber diameter

In this case and when we vary only the diameter of the absorber, the permeate flow also varies. This evolution was due to the increase of the exchange surface provided by the fiber with the increase of the absorber diameter. In addition, the increase of the absorber diameter increases its solar collector surface. Therefore, the power absorbed by the absorber will be better. Based on these two reasons, an enhancement of the heat and mass transfer was noted and the permeate flux tends to increase. However, when the absorber diameter increases the feed flow rate, outside of the fibers will undergo a drop. This influences the convection heat transfer between the absorber and feed. In addition, when the absorber diameter increases, the power lost by the absorber outer surface also increases. So, if we try to see only the last two findings when the absorber diameter increases the permeate flow rate decreases. Now, if we globalize our approach, we concluded that it is important to determine the absorber optimal diameter that provides a maximum permeate flow rate. To do this, we varied only the diameter of the absorber between 3 and 25

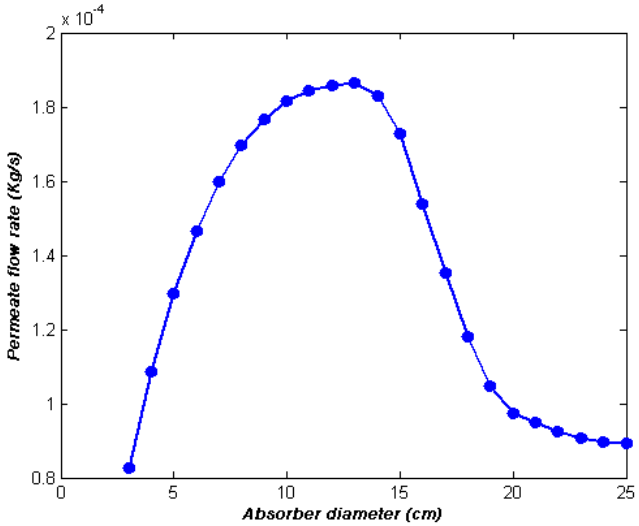

Figure 8. Permeate flow rate vs. Absorber diameter.

cm, and we calculated the permeate flow rate. Figure 8 demonstrates the impact of the absorber diameter on the permeate flow rate. According to this figure, the permeate flow rate increases to reach its maximum value for an absorber diameter of about 14 cm.

At this value, the permeate flow rate is about 18.6 10^{-5} kg/s. Then the permeate flow rate tends to decrease with increasing absorber diameter up to 23 cm to stabilize after that at a rate which is around 9 10^{-5} kg/s. In addition, it is important to see the evolution of the useful heat flow with the absorber diameter (Figure 9 (a)). From this figure, we showed that, when the absorber diameter increases, the solar collector surface also increases. Thus, the absorbed solar power is proportional to the collector surface. In addition, this figure shows the augmentation of the power loss with the increase of the absorber diameter and tends towards an asymptotic value of about 330 W when this diameter exceeds 18 cm. This change in the power loss can be explained by the fact that, when the absorber diameter exceeds 18 cm, the absorber outer wall temperature has a fixed value of 100 °C (Figure 9 (b)). The difference between the solar incident power and the heat flow loss is the useful heat flow. The evolution of this useful heat flow is proportional to the absorber diameter. However, when the diameter increases, the flow area allowed to the feed flow increases also. This leads to a drop in the average of the feed flow velocity (Figure 9 (c)). This drop influences the heat transfer coefficient between the interface feed/membrane (Figure 9 (b)). This coefficient has large values for the case of small diameter, but low permeate flux obtained in this case is due to the low temperature of the outer wall.

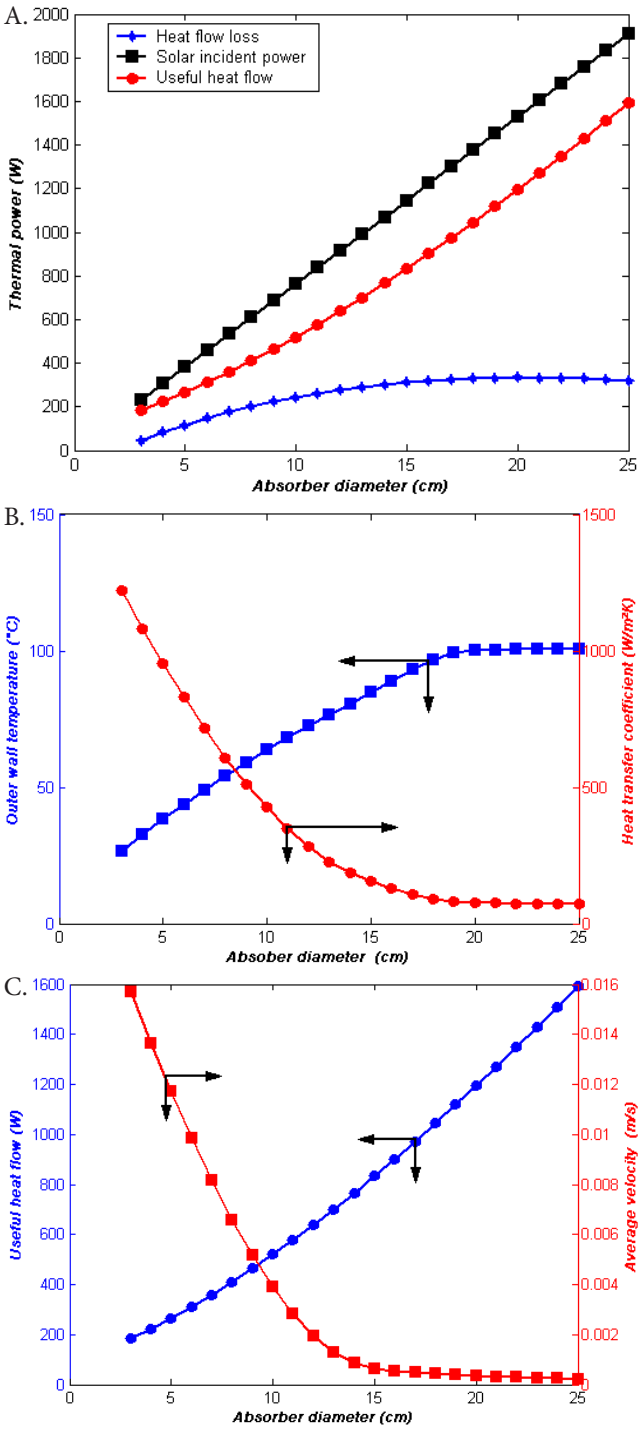

Figure 9. Effect of absorber diameter on (a) Solar incident power, heat flow loss and useful heat flow, (b) Outer wall temperature and heat transfer coefficient, (c) Average feed velocity and useful heat flow.

CONCLUSIONS

Numerical simulations have been done for a vacuum membrane installation coupled with solar energy and using a helically coiled fiber. This numerical simulation is based on a model composed of a system of non-linear equations allowing the coupling of simultaneous heat and mass transfer. These equations were solved using Matlab and FemLab software. To improve the performance of this installation, the effects of four operating parameters on the permeate flow rate were studied. These parameters are coil pitch, fiber diameter, distance between fiber and absorber internal wall and absorber diameter. After the simulation, we got the best values of these parameters, allowing us to maximize the permeate flow rate. These values were 3.22 cm for the coil pitch, 6 mm for the fiber diameter, 4.3 mm for the distance between fiber and the absorber internal wall and 14 cm for the absorber diameter. The obtained permeate flow rate was 18.6 × 10^{-5} kg/s when we use the above best values of the operating parameters. These best values will be used for the design of the installation to validate the developed model.

NOMENCLATURE

C_g Geometric concentration

d	Diameter, m
R_c	Coil radius, m
e	Thickness of the wall absorber, m
h_f	Boundary layer heat transfer coefficient of feed, W/m²K
I	Incident radiation on the level of the concentrator, W/m²
J_v	Permeate flux, kg/sm²
k_m	Membrane permeability coefficient, s $mole^{1/2}$ m^{-1} $kg^{-1/2}$
L	Module length, m
Lc	Length coil, m
L_v	Latent heat of vaporization, kJ/kg
m_{ij}	Feed flow rate in the inlet of element "j ", kg/s
m_{pi}	Permeate flow rate, kg/s
m_{oj}	Feed flow rate in the outlet of element "j ", kg/s
M_w	Water molar mass, kg/mol
P	Pressure, Pa / Pitch, m
P_{inter}	Water vapor pressure at the liquid/vapor interface, Pa
P_v	Vacuum pressure, Pa
q_a	Incident power of the absorber radiance, W/m²
q_e	Heat flow loss, W/m²
q_u	Useful heat flow, W/m²
r	Radial coordinate
R	Absorber radius, m
s_i	Outer side surface of the element "i" of the absorber, m^2
T	Temperature, K
u_r	Radial velocity, m/s
u_z	Axial velocity, m/s
w_s	Wind velocity, m/s
z	Axial coordinate

Greek

ε_a	Emissivity of the absorber
γ	Interception coefficient of absorber/ Dimensionless pitch
λ_m	Thermal conductivity of the absorber enlightened face, W/mK
ν	Kinematic fluid viscosity, m²/s
ρ	Reflectivity coefficient of the concentrator
σ	Stefan-Boltzmann constant, W/m²K^4
τ	Transmission coefficient of the glass cover of the absorber

Subscript

a	Ambient
bulk	Bulk
e	Absorber external wall
fij	Fluid at the entrance of the element "ji" of the absorber
foj	Fluid at the exit of the element "j" of the absorber
in	Inlet
inter	Interface membrane/feed
o	Out
w	Wall

REFERENCES

Ali, A., Aimar, P., Drioli, E. Effect of module design and flow patterns on performance of membrane distillation process. Chemical Engineering Journal, 277, 368-377 (2015). https://doi.org/10.1016/j.cej.2015.04.108

Andrjesdóttir, Ó., Ong, C.L., Nabavi, M., Paredes, S., Khalil, A.S.G., Michel, B., Poulikakos, D. An experimentally optimized model for heat and mass transfer in direct contact membrane distillation. International Journal of Heat and Mass Transfer, 66, 855-867 (2013). https://doi.org/10.1016/j.ijheatmasstransfer.2013.07.051

Bird, R.B., Lightfoot, E. N., Stewart, W.E. Transport phenomena. 2nd edition, Wiley, New York (2002).

Cabassud, C., Wirth, D. Membrane distillation for water desalination: how to choose an appropriate membrane? Desalination, 157, 307-314 (2003). https://doi.org/10.1016/S0011-9164(03)00410-7

Chaouchi, B., Zrelli, A., Gabsi, S. Desalination of brackish water by means of a parabolic solar concentrator. Desalination, 217, 118-126 (2007). https://doi.org/10.1016/j.desal.2007.02.009

Frikha, N., Benabdallah, B., Gabsi, S. Theoretical study of various configurations of solar desalination by vacuum membrane distillation. Desalination and Water Treatment, 83, 184-192 (2017). https://doi.org/10.5004/dwt.2017.21084

Gallet, P., Papini, F., Peri, G. Physique des convertisseurs héliothermiques. Edisud, Aix en Provence (1980).

Gong, X., Wang, F., Wang, H., Tan, J., Lai, Q., Han, H. Heat transfer enhancement analysis of tube receiver for parabolic trough solar collector with pin fin arrays inserting. Solar Energy, 144, 185-202 (2017). https://doi.org/10.1016/j.solener.2017.01.020

Izquierdo-Gil, M.A., Jonsson, G. Factors affecting flux and ethanol separation performance in vacuum membrane distillation (VMD). Journal of Membrane Science, 214, 113-130 (2003). https://doi.org/10.1016/S0376-7388(02)00540-9

Joo, H.-J., Kwak, H.-Y. Experimental evaluation for the freshwater production characteristics according to the salinity conditions of vacuum membrane distillation module. Desalination and Water Treatment, 57, 10005-10011 (2016). https://doi.org/10.1080/19443994.2015.1040267

Khayet, M. Membranes and theoretical modeling of membrane distillation: A review. Advances in Colloid and Interface Science, Membrane Separation and Colloid Science, 164, 56-88 (2011). https://doi.org/10.1016/j.cis.2010.09.005

Liu, S.H., Luo, G.S., Wang, Y., Wang, Y.J. Preparation of coiled hollow-fiber membrane and mass transfer performance in membrane extraction. Journal of Membrane Science, 215, 203-211 (2003). https://doi.org/10.1016/S0376-7388(02)00614-2

Mallubhotla, H., Schmidt, M., Lee, K.H., Belfort, G. Flux enhancement during Dean vortex tubular membrane nanofiltration: 13. Effects of concentration and solute type1. Journal of Membrane Science, 153, 259-269 (1999). https://doi.org/10.1016/S0376-7388(98)00255-5

Mendez, D.L.M., Castel, C., Lemaitre, C., Favre, E. Improved performances of vacuum membrane distillation for desalination applications: Materials vs process engineering potentialities. Desalination, 452, 208-218 (2019). https://doi.org/10.1016/j.desal.2018.11.012

Mengual, J.I., Khayet, M., Godino, M.P. Heat and mass transfer in vacuum membrane distillation. International Journal of Heat and Mass Transfer, 47, 865-875 (2004). https://doi.org/10.1016/j.ijheatmasstransfer.2002.09.001

Mericq, J.-P., Laborie, S., Cabassud, C. Vacuum membrane distillation of seawater reverse osmosis brines. Water Research, 44, 5260-5273 (2010). https://doi.org/10.1016/j.watres.2010.06.052

Nakoa, K., Date, A., Akbarzadeh, A. DCMD modelling and experimental study using PTFE membrane. Desalination and Water Treatment, 57, 3835-3845 (2016). https://doi.org/10.1080/19443994.2014.989272

Nariyoshi, Y.N., Pantoja, C.E., Seckler, M.M. Evaluation of sodium chloride crystallization in membrane distillation crystallization applied to water desalination. Brazilian Journal of Chemical Engineering, 33, 675-690 (2016). https://doi.org/10.1590/0104-6632.20160333s20150133

Qtaishat, M.R., Banat, F. Desalination by solar powered membrane distillation systems. Desalination, 308, 186-197 (2013). https://doi.org/10.1016/j.desal.2012.01.021

Sacadura, J. F. Initiation aux transferts thermiques, 2ème tirage, Technique et documentation, Paris (1980).

Safavi, M., Mohammadi, T. High-salinity water desalination using VMD. Chemical Engineering Journal, 149, 191-195 (2009). https://doi.org/10.1016/j.cej.2008.10.021

Salimpour, M.R. Heat transfer coefficients of shell and coiled tube heat exchangers. Experimental Thermal and Fluid Science, 33, 203-207 (2009). https://doi.org/10.1016/j.expthermflusci.2008.07.015

Salimpour, M.R. Heat transfer characteristics of a temperature-dependent-property fluid in shell and coiled tube heat exchangers. International Communications in Heat and Mass Transfer, 35, 1190-1195 (2008). https://doi.org/10.1016/j.icheatmasstransfer.2008.07.002

Shirazi, M.M.A., Kargari, A., Tabatabaei, M. Sweeping gas membrane distillation (SGMD) as an alternative for integration of bioethanol processing: study on a commercial membrane and operating parameters. Chemical Engineering Communications, 202, 457-466 (2015). https://doi.org/10.1080/00986445.2013.848805

Singh, D., Sirkar, K.K. Desalination by air gap membrane distillation using a two hollow-fiber-set membrane module. Journal of Membrane Science, 421, 172-179 (2012). https://doi.org/10.1016/j.memsci.2012.07.007

Wang, Y., Xu, Z., Lior, N., Zeng, H. An experimental study of solar thermal vacuum membrane distillation desalination. Desalination and Water Treatment, 53, 887-897 (2015).

Yücel, H., Çulfaz-Emecen, P.Z. Helical hollow fibers via rope coiling: Effect of spinning conditions on geometry and membrane morphology. Journal of Membrane Science, 559, 54-62 (2018). https://doi.org/10.1016/j.memsci.2018.04.048

Zrelli, A., Chaouachi, B., Gabsi, S. Simulation of a solar thermal membrane distillation: Comparison between linear and helical fibers. Desalination and Water Treatment, 52, 1683-1692 (2014). https://doi.org/10.1080/19443994.2013.807033

APPENDIX

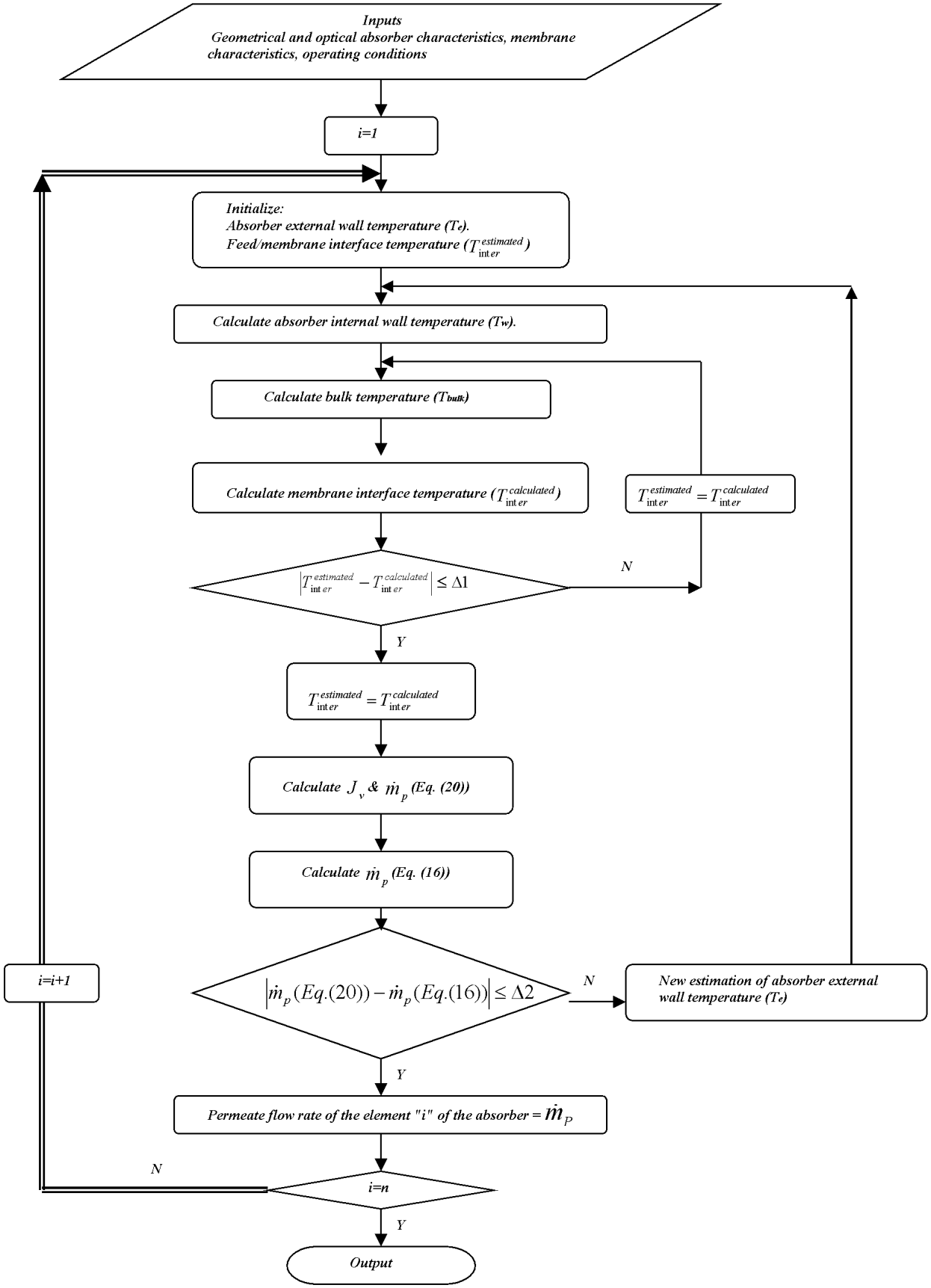

Figure A1. Algorithm used to calculate permeate flow rate.